01 Jan 2006

Modeling of Bioinspired Sensors for Flow Separation Detection for Micro Air Vehicles

Belinda A. Batten

John R. Singler
Missouri University of Science and Technology, singlerj@mst.edu

Benjamin T. Dickinson

Modeling of Bioinspired Sensors for Flow Separation Detection for Micro Air Vehicles

Ben T. Dickinson*, John R. Singler†, and Belinda A. Batten‡
Oregon State University, Corvallis, OR, 97331, USA

Autonomous micro air vehicle (MAV) flight faces inherent stability challenges. One challenge is controlling flow separation over the airfoil and an autonomous control system for MAV flight may be enhanced with closed loop separation control. In this work, we focus on modeling biologically inspired hair cell sensors for future flow control applications. We model the sensor output and present examples and numerical results.

Nomenclature

$\mathbf{u}$	flow velocity vector
p	pressure
ν	kinematic viscosity
$\mathbf{f}$	forcing on flow due to cilia sensor
Re	Reynolds number
$r(t,y)$	deflection of cilia sensor at time t and height y
ℓ	length of sensor
d	diameter of sensor
ρ	density
A	cross-sectional area of sensor
γ	Kelvin-Voigt damping coefficient for sensor
E	Young's modulus
I	moment of inertia
$g(t,y)$	distributed load intensity on a sensor at time t at height y
κ	proportionality constant for sensor output
C_f	drag coefficient for infinite cylinder
Subscripts	
t, y	partial derivatives with respect to time t and height y, respectively

I. Introduction

The utility of micro air vehicles (MAVs) in reconnaissance and surveillance applications is well established. Not only are there military applications that will lead to increased safety of the soldier in the field, but there are also beneficial civilian applications such as search and rescue, mobile weather stations, and environmental monitoring. Currently, overall utility is limited by non-autonomous (remote) control systems. The development of an autonomous MAV could increase their usefulness, however controlling inherent MAV instability must be addressed. One source of instability is in flow separation. A closed-loop separation control system may increase flight stability and enable the successful development of a truly autonomous MAV.

*Graduate Student, Department of Mechanical Engineering, 204 Rogers Hall, Member AIAA
†Research Associate, Department of Mechanical Engineering, 204 Rogers Hall, Member AIAA
‡Professor and Department Head, Department of Mechanical Engineering, 204 Rogers Hall, Member AIAA (formerly Belinda B. King)

Closed-loop flow control algorithms for stabilization of MAV flight require novel sensors due to payload and power limitations, as well as performance and robustness requirements. Our ultimate goal is to sense flow behavior above the airfoil. To this end, we consider biologically inspired hair-cell sensors developed by our partners in this research at the Micro Actuator Systems and Sensors (MASS) group at the University of Illinois at Urbana Champaign (see Figure 1). These sensors are similar in concept to hair cell sensors that

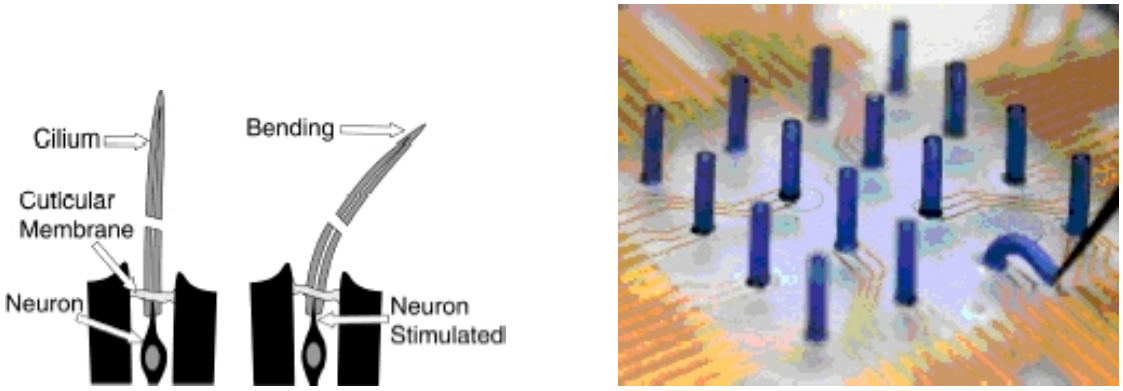

Figure 1. Biological cilia (left); Bio-inspired cilia array (right). *Figures courtesy of C. Liu and group, MASS lab, University of Illinois Urbana Champaign*

can be found on wings of certain insects; they may have a variety of roles including affecting flow as well as sensing flow characteristics. The work described in this paper is a precursor to investigating the utility of these sensors for flow separation detection. An example of the kind of flexible wing MAV for which we eventually plan to build a full control system is shown in Figure 2.

Figure 2. Flexible wing MAV.

As a first step toward developing a controller that would utilize this sensor output, we focus on modeling the output of a sensor developed by the MASS group. We model a sensor as a flexible rod and study how the flow impacts the sensor dynamics and output. Previous research on the topic modeled the sensor as a rigid rod and considered only steady flow. Details of our approach are discussed in Sections II and III. Sections IV and V present numerically computed sensor output for Blasius flow and flow over a backward step, respectively. We show how sensor output depends on a variety of characteristics including position in the flow and sensor height. We close with conclusions and questions for future research.

II. Development of a Dynamic Model for the Fluid-Sensor System

When we refer to a dynamic model for our MAV with cilia sensors, we refer to a coupled set of equations for the flow around the MAV, and for the sensor response to the flow. The starting point for model development will be the full set of coupled partial differential equations that arise from the physics.

The Navier-Stokes equations serve as the governing equations for the behavior of the fluid flowing around an airfoil. For simplicity, we consider flow in two dimensions. The presence of the cilia on the airfoil will create a disturbance in the flow. We model this disturbance by adding a small forcing term to the equations of motion. In nondimensional form, the equations can be written as

$$\begin{aligned} \mathbf{u}_t + (\mathbf{u}\cdot\nabla)\mathbf{u} - \nabla p - \frac{1}{Re}\nabla^2\mathbf{u} + \mathbf{f} = \mathbf{0}, \\ \nabla\cdot\mathbf{u} = 0, \end{aligned} \tag{1}$$

where $\mathbf{u}(t,\mathbf{x}) = [u(t,\mathbf{x}), v(t,\mathbf{x})]^T$ is the flow velocity vector in two dimensions, $\mathbf{x} = [x,y]^T$ is the spatial variable, t denotes time, $\mathbf{f}(t,\mathbf{x})$ is the body force due to the cilia, p represents pressure, and Re is the Reynolds number. The equations are supplemented with appropriate boundary conditions and an initial flow field.

When the cilia sensors are deformed due to a force, a voltage is induced through piezoresistive patches at the base (see Figure 1). As airflow sensors on a MAV wing, the cilia will produce such voltages due to bending moments induced by the forces resulting from loading of the cilia by the flow field. In all likelihood, there will be little damping due to air resistance in this application due to the size of the cilia; however, there may be material damping, for which we use a Kelvin-Voigt model. To capture this behavior, we turn to transverse displacement of a flexible rod. This leads to the following equation for each cilia sensor located at position $\mathbf{x}_i$

$$\rho A r_{tt}(t,y) + \gamma I r_{tyyyy}(t,y) + EI r_{yyyy}(t,y) = g(t,y), \tag{2}$$

with boundary conditions

$$\begin{aligned} r(t,0) = 0, \quad r_y(t,0) = 0, \\ EIr_{yy}(t,\ell) + \gamma I r_{tyy}(t,\ell) = 0, \quad EIr_{yyy}(t,\ell) + \gamma I r_{tyyy}(t,\ell) = 0, \end{aligned}$$

and sensor output

$$\eta(t) = \kappa\frac{d}{2}(Er_{yy}(t,0) + \gamma r_{tyy}(t,0)), \tag{3}$$

where $r(t,y)$ denotes the displacement of the cilia, ℓ is the length of the cilia sensor, d is the diameter, ρ is the density, A is the cross-sectional area, E is Young's modulus, I is the moment of inertia, γ is the coefficient of material damping, $g(t,y)$ is the distributed load intensity on the cilia at time t and height y, κ is an experimentally determined proportionality constant, and $\eta(t)$ is the voltage produced by the load on the sensor. We discuss the derivation of the equation for the sensor output in Section III.

In the future, we want to use the coupled equations for the flow (1), cilia deflection (2)-(3), and sensor output (3) to study the capability of the cilia sensors for feedback flow control. Before we can consider this, however, we must characterize the forcing on the cilia due to the flow and vice versa. In this work, we suppose that the flow velocity is small enough to neglect the effects of the cilia on the flow, i.e., we set $\mathbf{f} = \mathbf{0}$ in the Navier-Stokes equations (1). In the next section, we discuss the forcing that the flow exerts on a cilia sensor and the resulting sensor response.

III. Characterizing the Sensor Output

A. Forces Acting on a Sensor

In order to characterize the sensor output, we first must identify the forces acting on a cilia sensor. We use a local drag coefficient approach to estimate the surface forces; our approach is similar to the technique used in reference 1. As the sensors developed by the MASS group are cylindrical in shape, we model the geometry of a sensor as a right cylinder of uniform cross section and of finite height. To simplify the presentation, we focus on characterizing the sensor output when the sensor is mounted to a flat surface. We develop the equations in three dimensions, yet will simplify to the two dimensional case to use in the above model

scenario. In particular, assume the base of the sensor lies in the x-z plane and the sensor extends in the y direction from $y = 0$ to $y = \ell$.

Let $\mathbf{u}(t, \mathbf{x}) = [u(t, \mathbf{x}), v(t, \mathbf{x}), w(t, \mathbf{x})]^T$ be the three dimensional flow velocity vector. In this work, we suppose the flow is nearly two dimensional in character, i.e., we assume $w(t, \mathbf{x})$ is nearly constant for all t and $\mathbf{x}$. The anticipated forces to give the greatest sensor response are those acting perpendicular to the sensor's length (i.e., the forces due to the u velocity component which acts in the x direction). Let $\bar{u}(t, y) = u(t, x, y, z)$, where the positions x and z are chosen near but outside the influence of the sensor. Divide the cylinder into sections of height Δy_i for $i = 1, \ldots, n$ and let y_i be any point in the i^{th} section. Neglecting all other lift and drag forces, the drag force present on the i^{th} section may be approximated by

$$F_D(t, y_i) \approx \operatorname{sgn}(\bar{u}) \frac{1}{2} C_f(\bar{u})\, \rho\, d\, \bar{u}^2(t, y_i) \Delta y_i, \tag{4}$$

where ρ is the fluid density, d is the diameter of the sensor, and $C_f(\bar{u})$ is the local drag coefficient for an infinite cylinder in cross flow. The factor $\operatorname{sgn}(\bar{u})$ is included in the formula to account for the direction of the flow. Logarithmically interpolating experimentally determined drag coefficients[2] versus the Reynolds number, Re, for $Re < 10$ gives

$$\ln C_f(\bar{u}) \approx -0.67 \ln Re_{\text{loc}}(\bar{u}) + 2.51,$$

where the local Reynolds number is given by

$$Re_{\text{loc}}(\bar{u}) = \bar{u}(t, y_i) d / \nu,$$

ν is the kinematic viscosity of the fluid, and d is the diameter of the sensor.

This approach allows us to approximate the force at any point on the sensor. The total drag force over the length of the cilia can also be computed by summing the local drag forces $F_D(t, y_i)$ and taking the limit as $\Delta y = \max \Delta y_i$ tends to zero to obtain

$$F_{\text{total}}(t) = \int_0^\ell \operatorname{sgn}(\bar{u}) \frac{1}{2} C_f(\bar{u})\, \rho\, d\, \bar{u}^2(t, y)\, dy. \tag{5}$$

These expressions serve as approximations to the true forces acting on a sensor. One source of error in this analysis comes from the use of the drag coefficients. Cylinders of finite height have smaller drag coefficients compared to cylinders of infinite height.[2] This result is attributed to the disturbance of the fluid on the downstream side of the sensor caused by air passing around the end of the cylinder. Although finite cylinders show less resistance, for the unusually low cylinder Reynolds numbers in our analysis the end of the sensor is anticipated to have a negligible influence on the surrounding fluid. Finally, we have neglected lift forces which would induce axial stress on the sensor. The effects of lift will be considered in future work.

B. Computing the Sensor Output

A recent report on the mechanics of a cilia sensor made by the MASS group may be found in reference 3. A two axis force sensitive resistor (FSR) is integrated into the base of a polyurethane hair cell. Together, they comprise the cilia sensor. Net drag and lift forces from incident flow create a resultant moment at the sensor's base. The moment is conserved by compressive and tensile forces at the interface of the FSR and polyurethane material. The compressive and tensile forces act normal to the FSR and create a change in resistance $\Delta R/R$. By integrating the FSR into a bridge circuit, one can observe the resistance and small changes in the resistance.

By assuming the sensor output is linearly dependent on the average stress acting on the surface of the FSR element, a relation between the moment at the sensor's base and percent change in resistance may be obtained. From fundamental mechanics, the stress acting on the base of a cantilever beam at time t is given by

$$\sigma_{\text{base}}(t) = \frac{M(t) x}{I} \tag{6}$$

where $M(t)$ is the moment acting on the base at time t, x is the distance from the neutral axis, and I is the moment of inertia for a circular cross section. The actual FSR element is near the edge of the base and the stress, $\sigma_{\text{base}}(t)$, varies over its surface. As an approximation, let the FSR response be proportional to an

average stress represented by evaluating equation (6) at the edge of the base. Inserting the sensor's radius $d/2$ into equation (6) gives

$$\sigma_{\text{avg}}(t) \approx \frac{M(t)d}{2I}.$$

Assuming a linear relation between sensor output, $\eta(t)$, in the form of percent change in resistance and $\sigma_{\text{avg}}(t)$ gives

$$\eta(t) = \kappa\, \sigma_{\text{avg}}(t) = \kappa \frac{M(t)d}{2I}, \tag{7}$$

where κ is a proportionality constant dependent on the material properties of the sensor with units of $\mathrm{m\,s^2/kg}$. Due to the assumed Kelvin-Voigt damping mechanism, the moment at the base of the sensor is given by

$$M(t) = EIr_{yy}(t,0) + \gamma I r_{tyy}(t,0).$$

Substituting this expression into equation (7) gives equation (3) for the sensor output reported in Section II:

$$\eta(t) = \kappa \frac{d}{2I} M(t) = \kappa \frac{d}{2}(Er_{yy}(t,0) + \gamma r_{tyy}(t,0)).$$

To compute the moment at the base of the cilia, we need to approximate the solution of the beam equation (2)-(3) with the appropriate load on the cilia per unit length, $g(t,y)$. Equation (4) gives an approximation to the forces acting on a sensor at any point y along the height of the sensor and at any time t. The load distribution intensity (force per unit length) at each section of the sensor, $g(t,y_i)$, may be evaluated as

$$g(t,y_i) = F_D(t,y_i)/\Delta y_i \tag{8}$$

where Δy_i is the height of the i^{th} section. Equation (8) is obtained by equating the moment contributed by the resultant force acting in the center of the i^{th} section to the integral expression for moment. This may be written as

$$g(t,y_i) \int_{y_{i-1}}^{y_i} y\, dy = F_D(t,y_i)\, \bar{y}_i$$

where $\bar{y}_i$ is the moment arm length and $g(t,y_i)$ may be factored if the force distribution is assumed to be piecewise constant along the beam.

The beam model in (2)-(3) with $g(t,y)$ defined above in (4) and (8) is discretized in space using the finite element method with cubic B-splines and 16 equally spaced nodes. Details of the implementation can be found in reference 4. The resulting approximating ODE system is converted into first order form and solved using the trapezoid rule with a time step of 10^{-3}.

For our computations, we assumed the sensors are constructed of a polyurethane elastomer as in reference 3. In that work, the modulus of elasticity E for two different polyurethane elastomers was experimentally determined as 500 kPa and 20000 kPa. For our computations we used $E = 20000$ kPa. The density of polyurethane elastomers varies; a reasonable estimate for many polymers is 1000 $\mathrm{kg/m^3}$ and this value was used for the numerical results presented below. The cilia length, ℓ, and damping constant, γ, were varied in the computations. The diameter, d, of the sensor was fixed at 50 μm; the cross-sectional area, A, and the moment of inertia, I, are determined from the value of the diameter. The proportionality constant κ was set to one. The parameters are summarized in Table 1.

IV. Example and Numerical Results: Blasius Flow

A. Description of Flow Problem

The geometry investigated in this section is a right cylinder of uniform cross-section and finite height attached to a flat plate. The height of the sensor varies from 500 to 1300 μm with a constant diameter of 50 μm. The geometry is subject to a steady uniform flow of air parallel to the plate which varies in magnitude from .1 m/s to 9.1 m/s.

For various distances from the plate's leading edge, the effect of free stream velocity, sensor location, and height on sensor response was investigated. Without the sensor, the steady flow is governed by the Blasius equation

$$ff'' + 2f''' = 0, \tag{9}$$

Table 1. Parameters used for computations in the beam equation (2)-(3)

Parameter	Value
ℓ	variable m
d	50 μm
ρ	1000 kg/m^3
A	$\pi(d/2)^2$ m^2
E	20000 kPa
I	$\pi d^4/64$ m^4
γ	variable kg/m s
κ	10^{-3} m s^2/kg

with boundary conditions

$$f(0) = f'(0) = 0, \quad f'(\infty) = 1.$$

Details on the Blasius equation, its limitations, and solution are found in most fundamental fluid mechanics texts. The solution of the Blasius equation was approximated using a numerical method discussed in reference 5. Assuming the presence of the sensor has little influence on neighboring upstream flow, the distribution of force along the length of the sensor was determined from the local drag coefficient analysis presented in Section III.

B. Blasius Results

Figure 3 shows sensor output in percent change of resistance versus steady tip deflection for a height of 500 μm placed 5 cm from the plate's leading edge. Experimental results of sensor response versus tip deflection presented in reference 3 match the linear form of the data in Figure 3. By adjusting the proportionality constant, κ, and the modulus of elasticity, E, our numerical simulation can match the experimental results presented in reference 3.

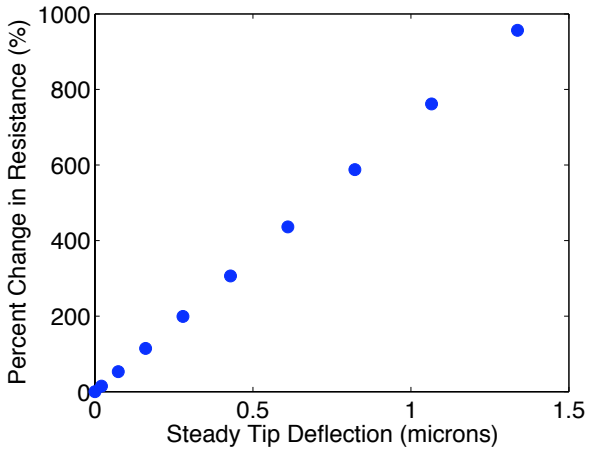

Figure 3. Sensor output vs tip deflection at 5 cm from the plate's leading edge and 500 μm tall sensor

Figure 4 demonstrates the steady sensor response vs free stream velocity for various heights of the sensor 10 cm from the leading edge of the plate. Figure 4 shows a roughly quadratic relationship between sensor output and free stream velocity. The sensitivity of sensor output with respect to free stream velocity is shown to increase as sensor height increases.

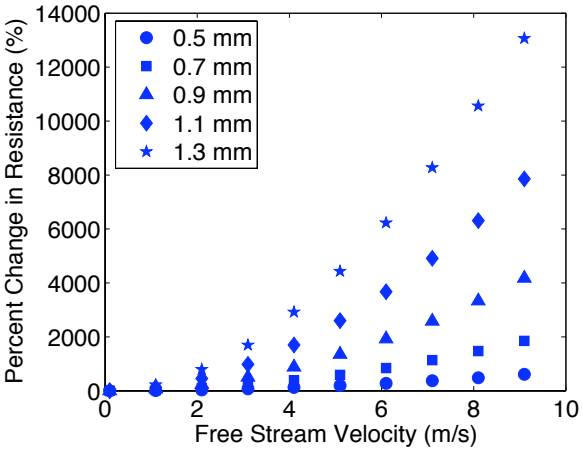

Figure 4. Sensor output versus free stream velocity for various sensor heights with position fixed at 10 cm from the leading edge

For a fixed sensor height, the increase in sensor output with increasing free stream velocity is attributed to an increase in drag force. By increasing the free stream velocity the boundary layer thickness decreases causing an increase in velocity gradient. This causes larger magnitude forces over the entire length of the sensor. As a result, a larger moment is created at the base leading to larger stresses on the FSR and thus a larger response by the sensor. In addition, increasing the sensor height is shown to increase the response of the sensor to the flow. This result is attributed to larger moments created at the sensor's base. Extending the sensor's height increases forces near the tip of the sensor, increases the moment arm length for these forces to act on, and increases the area for surface forces to act. Taller sensors may extend into the free stream placing the largest fluid velocities at the greatest distances from the base.

Figure 5 is a plot of sensor response to free stream velocity for various positions from the leading edge with the sensor height held constant at 500 μm. A decrease in the output sensitivity to free stream velocity for increasing distance from the leading edge can be seen.

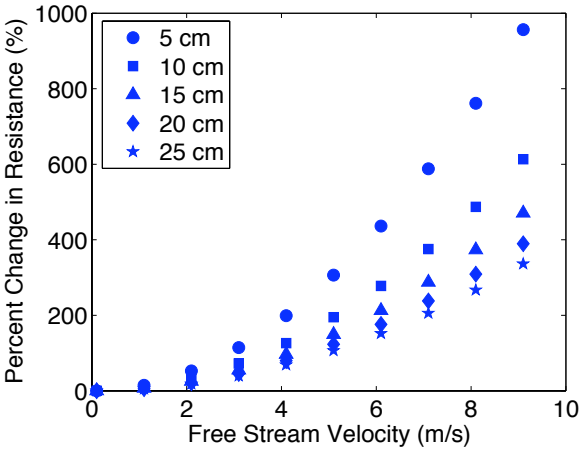

Figure 5. Sensor output versus free stream velocity for various positions from the leading edge with constant sensor height of 500 μm

By holding the position from the leading edge constant and varying height, the sensitivity (the change in output for change in free stream velocity) increases with increasing velocity. The increase in sensitivity is attributed to increasing forces concentrated in a region near the edge of the sensor. As mentioned in the

previous paragraph, the viscous region decreases with increasing free stream velocity causing sharper velocity gradients within the boundary layer. The sharper gradient and, in some cases, extension of the sensor into the free stream exposes the sensor's tip to greater fluid velocities. Since the drag force increases by a power greater than one with velocity, the resultant moment and thus response increases with increasing free stream velocity causing the increase in sensitivity that Figure 5 demonstrates.

From the previous results, the sensor output was shown to depend on height, position from the leading edge, and free stream velocity. A change in any one of these variables changes the velocities along the length of the sensor. From a different perspective, changing height, position, or velocity may be viewed as changing the thickness of the boundary layer. Thus, the sensor output to a change any of these variables may be expressed as a function of sensor height and boundary layer thickness. An investigation of steady sensor response from this perspective is a topic of future work.

V. Example and Numerical Results: Flow Over a Backward Step

For the flow over a plate considered in the previous section, we observed a roughly quadratic relationship between the free stream velocity and the steady output of the sensor. In this section, we numerically compute the sensor output for an unsteady flow over a backward facing step. Our experiments indicate that the unsteady sensor output does not appear to have a simple relationship to the flow nearby the cilia. In particular, changing the damping of the sensor can cause a large change in the sensor output.

The geometry of the backward facing step is shown in Figure 6. The main channel is 0.5 m long and 1 cm tall, and the inlet channel is 0.2 m long and 0.5 cm tall. A constant inflow velocity of 10 m/s is prescribed on Γ_{in} and the outflow condition $\partial\mathbf{u}/\partial\mathbf{n} = \mathbf{0}$ is set on Γ_{out}. On the other boundaries, we assume the flow satisfies the no-slip boundary condition $\mathbf{u} = \mathbf{0}$. The initial flow velocity is set to zero and the Reynolds number, Re, to 200.

Figure 6. Computational domain for flow over a backward facing step (not to scale); see the text for dimensions. The inflow and outflow boundaries are denoted Γ_{in} and Γ_{out}, respectively.

The solution of the Navier-Stokes equations (1) with $\mathbf{f} = \mathbf{0}$ was approximated using the finite volume method[6] as implemented in the StarCD software package. The flow initially is unsteady and small eddies develop due to the flow over the step. The flow becomes steady at approximately $t = 1$ s. For more details on this problem, see reference 7.

For the computations in this section, the sensor height and radius are fixed at 0.5 mm and 0.025 mm, respectively. The damping coefficient, γ, is varied in the simulations. The other sensor parameters are given in Table 1. As in the previous section, the sensor output is computed using equation (3) with $\kappa = 1$ mm s^2/kg. The forcing on the beam equation is computed using (4) and (8) as described in Section III. Unlike the Blasius flow computations, we do not fully resolve the flow in the boundary layer in order to compute the force acting on the sensor; instead, we simply use the value of the flow in the finite volume cell containing the cilia for the force calculations.

A sensor is placed on the bottom wall of the main channel 0.0175 m away from the lower left corner. The flow develops an eddy above the sensor. Figure 7 shows the computed flow velocity normal to the sensor and the computed distributed load intensity acting on the sensor. The distributed load intensity mimics the behavior of the normal flow velocity in time.

Figures 8 and 9 show the tip deflection of the sensor and the sensor output, respectively, for values of the damping coefficient γ of 10^5 and 10^6 kg/mm s. The change in the damping coefficient dramatically changes the transient behavior of the tip deflection and the sensor output. In particular, for $\gamma = 10^5$ kg/mm s the sensor output mimics the shape of the velocity acting normal to the sensor; however, for $\gamma = 10^6$ kg/mm s the sensor output no longer resembles the normal velocity. The magnitude of the sensor output also changes by an order of magnitude; this is a result of holding κ constant. Since κ depends on the material properties of the sensor (γ in particular), the magnitude of the output is most likely unrealistic. However, the difference in the *shape* of the output is significant.

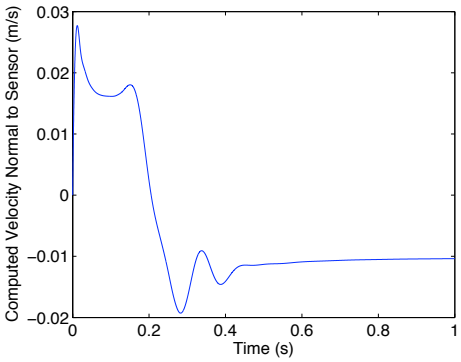

(a) Computed flow velocity normal to sensor

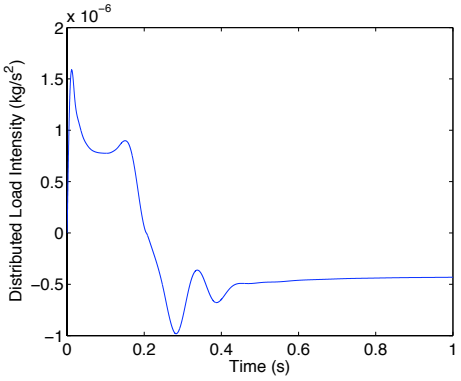

(b) Computed distributed load intensity acting on sensor

Figure 7. Sensor located on the bottom wall of the main channel near an eddy; see text for details.

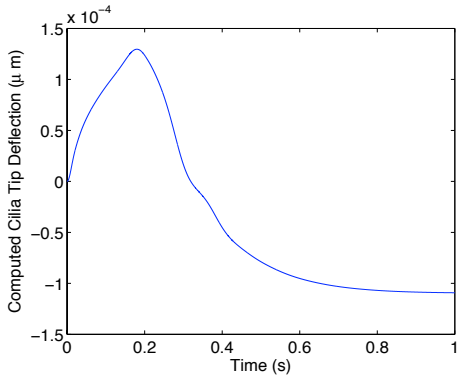

(a) $\gamma = 10^5$ kg/mm s

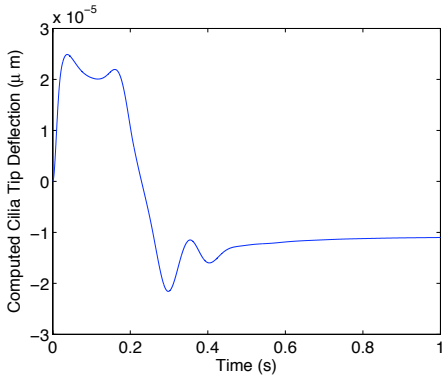

(b) $\gamma = 10^6$ kg/mm s

Figure 8. Computed tip deflection of sensor for two values of the damping coefficient γ.

At this point, it is not clear which damping coefficient produces a more desirable sensor output for a feedback control law. Though the sensor output with $\gamma = 10^5$ kg/mm s follows the normal velocity, the sensor output with $\gamma = 10^6$ kg/mm s may contain information that is more relevant for control purposes. The tip deflection with $\gamma = 10^6$ kg/mm s seems to be much more sensitive to small variations in the distributed load intensity acting on the sensor. This may indicate that the sensor output with $\gamma = 10^6$ kg/mm s provides more precise information. Once experimental data is obtained, parameter estimation studies should provide insight into an appropriate damping parameter. Future investigation into this matter could provide motivation for designing sensors with specific material properties.

VI. Conclusions and Future Work

In this paper, we have developed a model for a bio-inspired cilia sensor in a fluid that could be used for the purpose of sensing characteristics of the flow. This model starts from a coupled set of partial differential equations that includes the Navier-Stokes model of the fluid, and a flexible rod model for the sensor. A finite element approximation of the sensor is used along with a finite volume code for the flow computations to yield an approximating system that can be used for simulations. The computational data obtained is validated by experimental data provided in reference 3. We have provided data regarding sensor sensitivity with respect to height and position along a flat plate.

Once experimental data for these particular sensors is obtained in an unsteady flow, we will apply

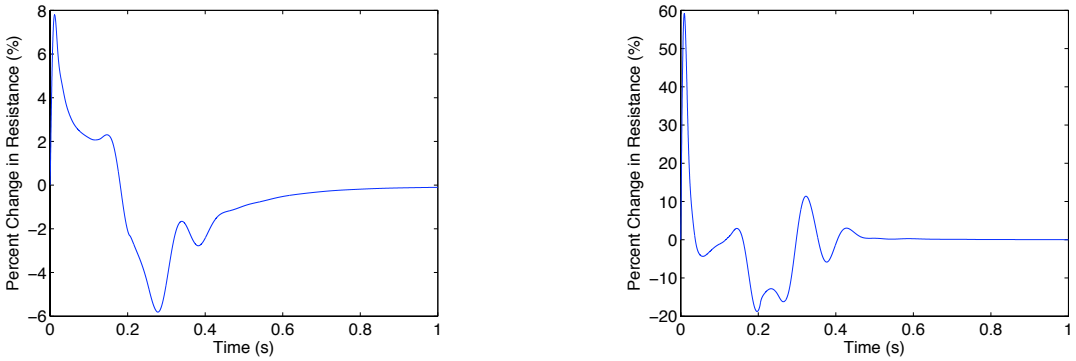

(a) $\gamma = 10^5$ kg/mm s (b) $\gamma = 10^6$ kg/mm s

Figure 9. Computed sensor output for two values of the damping coefficient γ.

parameter estimation to more accurately model the cilia parameters, particularly damping coefficients. We will then use these models as a starting point for reduced order models of the fluid-sensor system that can be used for the development of observers and controllers. In addition, the results regarding position and heights of the sensors will be used in construction of sensor arrays which can be applied to the problem of flow separation detection for MAVs. Once we have these arrays, the effect of the presence of the cilia on the flow will be modeled and tested experimentally.

Acknowledgments

Research supported in part by Air Force Office of Scientific Research under grants F49620-03-1-0326 and FA9550-05-1-0041. We also acknowledge the collaborative support and motivating problem provided by Prof. Chang Liu and the MASS group at the University of Illinois Urbana-Champaign.

References

[1]Fan, Z., Chen, J., Zou, J., Bullen, D., Liu, C., and Delcomyn, F., "Design and fabrication of artificial lateral line flow sensors," *Journal of Micromechanics and Microengineering*, Vol. 12, No. 5, 2002, pp. 655 – 661.

[2]Prandtl, L., *Essentials of Fluid Dynamics*, Hafner Publishing Company, New York, 1952.

[3]Engel, J., Chen, J., Chen, N., and Liu, C., "Development and characterization of an artificial hair cell based on polyurethane elastomer and force sensitive resistors," *The 4th IEEE International Conference on Sensors*, 2005, pp. 1014–1017.

[4]Prenter, P. M., *Splines and Variational Methods*, John Wiley & Sons, New York, 1989.

[5]Nunn, R. H., *Intermediate Fluid Mechanics*, Hemisphere Publishing Corporation, New York, 1989.

[6]Versteeg, H. and Malalasekra, W., *An Introduction to Computational Fluid Dynamics: The Finite Volume Method*, Prentice Hall, Harlow, England, 1996.

[7]Armaly, B. F., Durst, F., Pereira, J. C. F., and Schoenung, B., "Experimental and theoretical investigation of backward-facing step flow," *Journal of Fluid Mechanics*, Vol. 127, 1983, pp. 473 – 496.